Tellurium isotope fractionation during evaporation from silicate melts

Christian J. Renggli [a,*], Jan L. Hellmann [b,c], Christoph Burkhardt [b,d], Stephan Klemme [a], Jasper Berndt [a], Paul Pangritz [a], Thorsten Kleine [b,d]

[a] *Institut für Mineralogie, University of Münster, Münster 48149, Germany*
[b] *Institut für Planetologie, University of Münster, Wilhelm-Klemm Straße 10, 48149 Münster, Germany*
[c] *Now in: Department of Geology, University of Maryland, 8000 Regents Drive, College Park, MD 20742, USA*
[d] *Now: Max Planck Institute for Solar System Research, Justus-von-Liebig-Weg 3, 37077 Göttingen, Germany*

ARTICLE INFO

ABSTRACT

As a moderately volatile, redox-sensitive chalcophile and siderophile element, Te and its isotopic composition can inform on a multitude of geochemical and cosmochemical processes. However, the interpretation of Te data from natural settings is often hindered by an insufficient understanding of the behavior of Te in high-temperature conditions. Here, we present the results of Te evaporation and isotopic fractionation in silicate melting experiments. The starting material was boron-bearing anorthite-diopside glass with 1 wt% TeO_2. The experiments were conducted over the temperature range of 868–1459 °C for 15 min each, and at oxygen fugacities ($\log fO_2$) relative to the fayalite-magnetite-quartz buffer (FMQ) of FMQ–6 to FMQ+1.5, and in air. Evaporation of Te decreases with decreasing fO_2. For high-temperature experiments performed at >1200 °C Te loss is accompanied by Te isotope fractionation towards heavier compositions in the residual glasses. By contrast, Te loss in experiments performed at temperatures <1200 °C typically resulted in lighter Te isotopic compositions in the residues relative to the starting material. In air, Te evaporates as TeO_2, whereas at lower oxygen fugacities we predict the evaporation of Te_2, using Gibbs free energy minimization calculations. In air, the experimentally determined kinetic isotopic fractionation factor for $\delta^{128/126}$Te at T > 1200 °C is α_K = 0.99993. At reducing conditions, Te likely substitutes as Te^{2-} for O^{2-} in the melt structure and becomes increasingly soluble at highly reducing conditions. Consequently, Te evaporation is not predicted for volcanic processes on reduced planetary bodies such as the Moon or Mercury.

© 2022 Elsevier Ltd. All rights reserved.

1. Introduction

Tellurium is a redox-sensitive moderately volatile element and its distribution and isotopic composition in geologic and planetary materials can provide key insights into geo- and cosmochemical processes. These processes include the formation and evolution of planetary building blocks in the solar accretion disk, core formation, volcanic degassing, and the late accretion of planetary materials onto terrestrial bodies.

Tellurium has a 50% condensation temperature (50% T_C) in a gas of solar composition at 10^{-4} bar of ~700 K (Wood et al., 2019; Lodders, 2003). It naturally occurs in four oxidation states, as reduced telluride (-II), native tellurium (0), tellurite (+IV), and oxidized tellurate (+VI). The volatility and redox dependency control the elements' behavior in different geo- and cosmochemical settings.

In meteorites, Te exhibits highly variable behavior, reflecting meteorite parent body formation in distinct regions of the accretionary disk and under vastly different conditions (Kadlag and Becker, 2016a, 2017). While Te shows predominantly chalcophile behavior in carbonaceous chondrites (Kadlag and Becker, 2016b), it is largely siderophile in enstatite chondrites (Kadlag and Becker, 2015), and displays a complex behavior between chalcophile and siderophile in ordinary chondrites (Kadlag and Becker, 2016a, 2017). Moreover, Te is variably depleted in different meteorite groups relative to the solar composition, and meteorites exhibit large fractionation in Te isotopic compositions (Fehr et al., 2018; Hellmann et al., 2020, 2021). For instance, in carbonaceous chondrites, Te depletion and Te isotope fractionation are correlated, which has been interpreted to reflect mixing of volatile-rich, isotopically heavy CI-like dust with volatile-depleted, isotopically light chondrules or chondrule precursors (Hellmann et al., 2020). The volatile element budget and isotopic signature of the latter result, however from evaporation and/or condensation

processes, which are not tightly constrained. In enstatite chondrites, materials that underwent high-temperature thermal metamorphism are strongly depleted in Te and isotopically heavy relative to weakly- or unmetamorphosed samples, likely reflecting volatile element loss from the parent bodies (Hellmann et al., 2021). By contrast, ordinary chondrites display no correlations in metamorphic degree with Te depletion and isotope fractionation, although they are thought to have undergone similar parent body high-temperature thermal metamorphism as enstatite chondrites (Hellmann et al., 2021). Why Te behaves fundamentally differently in enstatite and ordinary chondrites remains poorly understood.

In the bulk silicate Earth (BSE), Te, as a chalcophile to siderophile element, is similarly depleted relative to CI chondrites as the other chalcogens S and Se (Palme and O'Neill, 2014). The concentration of Te in mid-ocean ridge basalts is below 10 ppb (Yi et al., 2000; Lorand and Alard, 2010; Lissner et al., 2014). Nevertheless, volcanic processes result in the enrichment of Te, and the formation of deposits, particularly including at fumarolic vents. These processes include the evaporation of Te from primary and evolved magmas, and the transport in a gas or fluid phase (Tombros et al., 2010; Henley and Berger, 2013; Grundler et al., 2013; Tombros and Fitros, 2019; Renggli and Klemme, 2020). Extensive volcanic degassing of Te can also be recorded in sediments, such as at the boundary between the late Permian and the early Triassic period. The observed Te anomaly is used as a proxy for the eruption of the Siberian flood basalts and the associated mass extinction event (Regelous et al., 2020). High emissions of Te in volcanic gases, relative to the magmatic source, are observed in diverse volcanic settings, but the gas phase enrichment is more pronounced in rift- and hotspot-related settings (Zelenski et al., 2021).

Impact cratering events can cause extensive melting and vaporization (Pierazzo et al., 1997). For example, lunar impact glasses are highly depleted in volatile and moderately volatile elements (Warren, 2008). However, the abundances and ratios of Te, Se, and S in lunar mafic impact melt breccias appear similar to those of pristine lunar mafic target rocks, such as mare basalts (Gleißner and Becker, 2020; Gleißner et al., 2022). The lack of a strong depletion signature may suggest that high-energy impacts like that forming the Imbrium basin did not cause significant evaporative loss of Te, Se, and S.

Earlier experimental work established the evaporation of metal cations and oxides from silicate melts as a function of variable oxygen fugacities (fO_2) and temperatures (Norris and Wood, 2017; Sossi et al., 2019). The effect of metal evaporation on the fractionation of stable isotopes is increasingly addressed using experimental approaches, such as for K, Mg, Cd, Cu, Zn, Tl, Ga, and Cr (Wombacher et al., 2004; Richter et al., 2007, 2009,2011; Wang and Jacobsen, 2016; Young et al., 2019; Wimpenny et al., 2019, 2020; Sossi et al., 2020; Nielsen et al., 2021; Neuman et al., 2022; Klemme et al., 2022). However, for the evaporation of elements that occur both as cation oxides, or as anions in silicate melts, very few fO_2-controlled experiments exist. These include experiments on Se evaporation in air from MORB basalts (Yierpan et al., 2021), and heating experiments of CM chondrite (Murchison) samples in air and Ar gas, including measurements of S, Te, and Se (Braukmüller et al., 2018). Braukmüller et al. (2018) observed increased evaporation of S and Se in O_2 compared to Ar gas, and a smaller fO_2 effect for Te, with a higher Te volatility in Ar gas compared to S and Se. However, fO_2 was not fully controlled in these experiments.

The above points reveal that the behavior of Te at high-temperature conditions remains poorly constrained, hampering the interpretation of Te elemental and isotope signatures in nature. To address this issue, here, we investigate Te evaporation experimentally at temperatures from 868 to 1459 °C, and as a function of fO_2 from six orders of magnitude below the Fayalite-Magnetite-Quartz buffer (ΔFMQ-6) to air, and determine the isotopic fractionation of Te.

2. Methods

2.1. Starting material and evaporation experiments

Tellurium evaporation experiments were run with a silicate melt that contained 1 wt% TeO_2. The composition was chosen at the anorthite-diopside eutectic composition, with the addition of 15 wt% B_2O_3. Boron was added to the mixture to reduce the liquidus temperature and allow experiments at temperatures below 1200 °C. The glass was synthesized from chemical grade oxides (MgO, SiO_2, Al_2O_3), carbonate ($CaCO_3$), and H_3BO_3. After decarbonation (1000 °C, 3 h) the mixture was molten at 1200 °C for 30 min in a Pt crucible in air and quenched in water. This initial Te-free glass was ground to a fine powder and a nominal amount of 1 wt% TeO_2 was added. Subsequently, the powder was mixed in an agate mortar for 45 min, vitrified for 7 min in a Pt crucible at 1200 °C, and quenched in water. The duration of 7 min was chosen to allow the formation of a glass and limit the evaporation of Te during synthesis of the glass (Pangritz et al., 2022). This synthesis process did not allow us to control the redox state of Te in the starting material, which would have resulted in significant Te-loss from the starting material prior to the degassing experiments. The glass was investigated on the scanning electron microscope and chemical homogeneity was confirmed by electron microprobe analysis (Fig. 1). Vesicles in the starting material are due to incomplete sintering in the final synthesis step (Pangritz et al., 2022). We determined a TeO_2 concentration of 0.96 ± 0.04 wt%, (n = 176, SiO_2 41.62(71), Al_2O_3 13.31(65), B_2O_3 15.35(57), CaO 19.85(39), MgO 7.50(27) wt.%, including line profiles and spots, see supplement for analysis of starting material).

The glass was broken into chips with diameters of 1–2 mm. The chips were hooked on Pt-wire with a diameter of 0.1 mm. For each run, two samples were suspended on a Pt-chandelier on an alumina rod, one for characterization with secondary electron microscopy (SEM), electron probe microanalysis (EPMA), and laser ablation inductively coupled plasma mass spectrometry (LA-ICP-MS), and a second sample for digestion and stable isotope analysis with MC-ICP-MS (see details on analytical methods below). Both samples experienced the same temperature and fO_2 conditions during the experiments. The experiments were conducted in a vertical gas-mixing tube furnace (Gero GmbH), with a gas volume of ~1160 cm^3, and oxygen fugacity was controlled by mixing CO and CO_2 gas at a gas flow rate of 100 cm^3 per minute. The samples were initially placed in the cold zone of the furnace to allow the CO-CO_2 gas mixture to equilibrate for ~2 min. The samples were then lowered into the hot zone of the furnace, where evaporative loss of Te occurred for 15 min, and quenched in water. We could not detect any Te in the Pt wire by EPMA after the experiments. Aliquots of the undegassed glass chip starting material were crushed to powder and their Te stable isotope composition was measured.

2.2. Sample characterization

Each experiment contained two samples, one of which was characterized in cross-section with a JEOL 6510 LA scanning electron microscopy (SEM), and the chemical composition was measured with a 5-spectrometer JEOL JXA 8530F electron microprobe analyzer (EPMA), and laser ablation inductively-coupled plasma mass spectrometry (LA-ICP-MS) at the Institut für Mineralogie, University of Münster (full data in supplement). The SEM
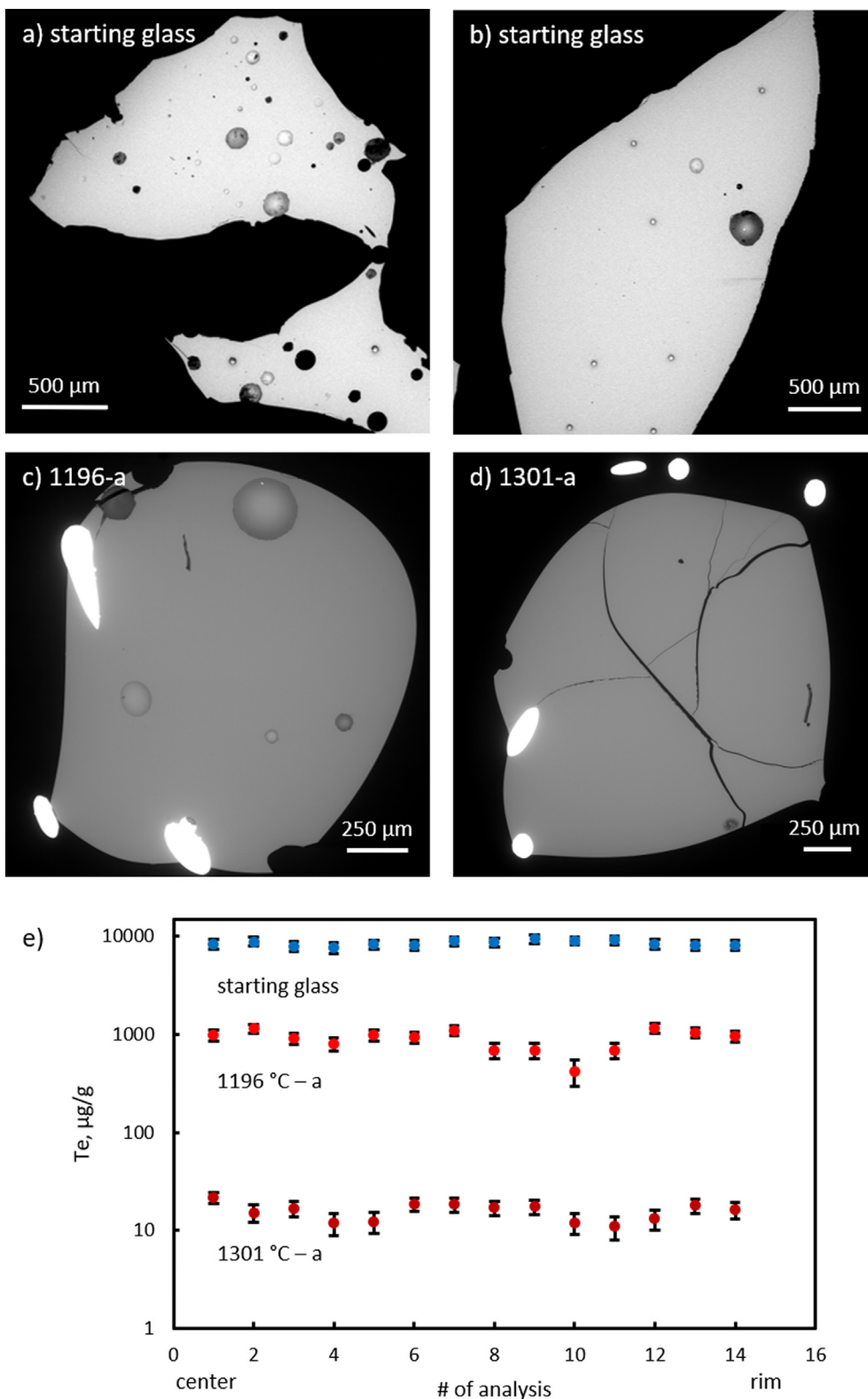
Fig. 1. Characterization of starting materials and experimental samples. (a) and (b) show BSE images of glass fragments of the starting material. Images (c) and (d) show BSE images of the polished cross-sections of experiments in air at 1196 °C and 1301 °C respectively. (e) LA-ICP-MS measurements on the starting glass, and profiles from the center of the experimental beads that are shown in c) and d). The profiles (75 μm step size) show no diffusional zonation from the center (analysis #1) to the rim (analysis # 14).

back-scattered electron images were taken at an acceleration voltage of 20 kV and a working distance of 10 mm.

The EPMA measurements were made at an acceleration voltage of 15 kV, 60nA beam current, and a 20 μm beam size. Tellurium

and B were measured for 120 s on the peak and 60 s on the background. Te was measured on two diffraction crystals (PETH and PETL) and we used a metallic Te standard (Ast_Te). The other elements (Ca, Mg, Si, Al) were measured for 20 s on the peak and 10 s on the background.

Polished samples were ablated in a dual-volume Helex cell (He gas flux of 1 L/min in the large cell and 0.33 L/min in the small cell) for LA-ICP-MS measurements. We used a Photon Machines Analyte G2 193 nm ArF excimer laser at a pulse rate of 10 Hz and a spot size of 50 μm for the sample ablation. Profiles were measured from core to rim of the samples at 75 μm steps. The ablated material was analyzed in a Thermo-Fisher Element XR, measuring 20 s background and 40 s sample counting time. The isotopes measured were ^{11}B, ^{29}Si, ^{43}Ca, and ^{125}Te, and ^{43}Ca was used as the internal standard. The primary standard analyzed was NIST610 (302.3 (6.8) ppm Te, n = 63), and we also measured the Te concentrations in NIST612 (34.8(1.9) ppm, n = 83) and BHVO-2G (at the detection limit of ~0.5 ppm Te). The results of the standard measurements are presented in the supplement.

2.3. Tellurium stable isotope measurements

Samples [evaporation experiment glasses, Te starting glass, and pure Te-oxide (DB01)] were individually weighed into 15 mL Savillex PFA vials and dissolved in 2:1 HF–HNO$_3$ on a hot plate for ~3 days at 120 °C. After dissolution, samples were evaporated and dried at 120 °C, and re-dissolved in concentrated HCl-HNO$_3$ and concentrated HNO$_3$ several times to destroy fluorides that may have formed during digestion. The samples were then converted to chlorides via several dry-downs in concentrated HCl, re-dissolved in 10 mL 2 M HCl, and equilibrated on a hotplate for ~12 h at 120 °C. Based on Te abundances determined on corresponding experiments by LA-ICPMS (see Section 2.2), 0.1–100% aliquots of the digested sample solutions were mixed with appropriate amounts of a ^{123}Te-^{125}Te double spike (Hellmann et al., 2020) and equilibrated on a hotplate for ~12 h at 120 °C. Experiment duplicates with low Te concentrations (1400b, 1450c, 1500c; 3.3–3.9 ng/g Te) were spiked prior to sample digestion to evaluate potential Te loss during sample dissolution, but have otherwise been treated like the other samples. Of note, the experiment duplicates and their equivalents that have been spiked after dissolution exhibit similar Te concentrations and isotope compositions, providing strong evidence that no significant amounts of Te were lost in the sample dissolution stage. Finally, all samples were evaporated to dryness at 120 °C and re-dissolved in 10 mL 2 M HCl for ion exchange chemistry.

Tellurium was separated from the sample matrix by ion exchange column chromatography (Hellmann et al. 2020). In brief, samples were loaded in 10 mL 2 M HCl onto pre-cleaned anion exchange columns filled with 5 mL BioRad AG1X8 resin (200–400 mesh). After sequential washes of 15 mL 2 M HCl, 7 mL 11 M HCl, and 15 mL 5 M HF, Te was eluted in 10 mL 1 M HNO$_3$. Organic components in the Te fraction were removed by dry-downs in concentrated HCl–HNO$_3$ and HNO$_3$. While samples with low Sb/Te ratios were then dissolved in 0.28 M HNO$_3$ for isotope measurements, samples with high Sb/Te ratios (>1 × 10^{-4}) were further processed through a clean-up ion exchange chemistry (Hellmann et al., 2020). They were evaporated to dryness, converted to chloride form by repeated dry-downs in concentrated HCl, and re-dissolved in 1 mL 2 M HCl. After loading the samples onto columns filled with pre-cleaned 1 mL BioRad AG1X8 resin (200–400 mesh), and sequential washing with 5 mL 2 M HCl, 2 mL 11 M HCl, and 5 mL 5 M HF, Te was eluted using 6 mL 0.5 M HCl. Finally, the samples were repeatedly dried down in HCl–HNO$_3$ and HNO$_3$ and then dissolved in 0.28 M HNO$_3$ for isotope measurements. Total procedural blanks are <20 pg Te, i.e.,

≪1% of the total Te amount in the processed samples, and therefore generally negligible.

Additionally, some of the pure Te-oxide powder used in the preparation of the starting glass (see Section 2.1), was dissolved in concentrated HNO$_3$ and was spiked with an appropriate amount of ^{123}Te-^{125}Te double spike. Then, the sample (DC01) was evaporated to dryness and dissolved in 0.28 M HNO$_3$ for isotope measurements without any further chemical purification.

All Te isotope measurements were performed using a ThermoScientific Neptune *Plus* multi-collector ICP-MS at the Institut für Planetologie at the University of Münster and followed the measurement routine described in Hellmann et al. (2020). Samples were introduced using a Cetac Aridus II desolvator and a Savillex C-flow nebulizer at an uptake rate of ~40 μl/min. Sample solutions were measured at ~100 ng/g Te using standard sampler and X skimmer cones. For a 100 ng/g Te standard solution this configuration yielded total ion beam intensities of ~2.5 × 10^{-10} A. Ion beams were collected simultaneously using Faraday cups connected to 10^{11} Ω feedback resistors for ^{123}Te, ^{125}Te, ^{126}Te, and ^{130}Te, and Faraday cups connected to 10^{12} Ω feedback resistors for ^{121}Sb and ^{129}Xe.

Prior to each analysis, the sample introduction system was washed using 0.28 M HNO$_3$ for 15 min. Each measurement consisted of on-peak background measurements of 100 × 1.05 s integrations, followed by sample measurements of 50 cycles of 4.2 s each. Constant isobaric interferences of Xe on ^{126}Te and ^{128}Te from the Ar gas were corrected using on-peak background measurements. Interferences of residual Sb (on ^{123}Te) and Xe were corrected iteratively using the exponential mass fractionation law, but were insignificant for all samples.

The measured raw data were processed off-line following the three-dimensional data reduction routine of Siebert et al. (2001), using $^{123}Te/^{128}Te$, $^{125}Te/^{128}Te$ and $^{126}Te/^{128}Te$. The double spike inversion provides the natural fractionation factor α, for which the Te stable isotopic composition of a sample is calculated as follows:

$$\delta^{128/126}Te_{sample} = -1000 \times (\alpha_{sample} - \alpha_{MeanNISTSRM3156})$$
$$\times \ln(m_{128}/m_{126}) \tag{1}$$

where m_{128} and m_{126} are the atomic weights of ^{128}Te and ^{126}Te and $\alpha_{Mean\ NIST\ SRM\ 3156}$ is the mean natural fractionation factor α of a spiked bracketing NIST SRM 3156 standard solution measured at similar concentrations in the same measurement sequence. Here, $\delta^{128/126}Te$ is defined as the permil deviation of the $^{128}Te/^{126}Te$ ratio of a sample from the composition of the NIST SRM 3156 Te standard:

$$\delta^{128/126}Te = \left[\frac{\left(^{128}Te/\ ^{126}Te \right)_{sample}}{\left(^{128}Te/\ ^{126}Te \right)_{SRM3156}} - 1 \right] \times 1000 \tag{2}$$

The results for samples are reported as the mean of replicate measurements (n = 3–5) with their corresponding two standard deviation (2 s.d.).

Throughout this study we use Te concentrations determined using the double spike method, because these analyzes represent measurements of the bulk sample (concentration and isotope composition were obtained from the same measurements), the precision is higher, and the detection limit is significantly lower than for Te concentration measurements performed using the microprobe or laser ablation ICPMS.

2.4. Tellurium isotopic composition of the starting material

The pure TeO$_2$, which has been used for the synthesis of the starting glass, was analyzed for its isotopic composition after being

processed in two different ways. First, the oxide processed in the same way as the experiments and starting glasses (see description above) exhibits a $\delta^{128/126}Te = 0.42 \pm 0.02$. Second, TeO_2 that was analyzed without prior chemical purification has a $\delta^{128/126}Te = 0.43 \pm 0.01$, which is the same value within uncertainty of the processed TeO_2. This demonstrates that Te isotopes remained unfractionated during sample digestion and repeated dry downs in different acids and acid mixtures outlined above.

Glass chips 2, 3, and 4 are homogeneous in their Te isotope compositions [average $\delta^{128/126}Te = 0.33 \pm 0.06$ (n = 4, ±2s.d.)] and exhibit Te concentrations of 6580–7589 μg/g (0.85–0.95 wt% TeO_2). Individual chips and a larger aliquot of powdered glass were analyzed to assess the isotopic homogeneity of the starting material. The powdered starting glass (∼21 mg aliquot of ∼200 mg powder) has a Te concentration of 7589 ± 139 μg/g and an isotope composition of $\delta^{128/126}Te = 0.33 \pm 0.01$. Glass 1 displays a lighter $\delta^{128/126}Te$ of 0.09, and a lower concentration of 6311 μg/g. The slightly lighter isotope compositions of the Te starting glasses relative to the pure TeO_2 likely result from Te isotope fractionation that occurred during production of the Te starting glass. However, replicates of evaporation experiments starting from different glass chips exhibit similar Te isotope systematics. To account for isotopic heterogeneities in the starting material we use the mean of the $\delta^{128/126}Te$ isotopic compositions of the glass powder and the glass chips 1–4 as the reference composition (Table 1).

We present the Te isotopic compositions of the experiments as $\Delta^{128/126}Te$, where the experimental data are normalized to the isotopic composition of the initial mean (glass powder and glass chips) with $\delta^{128/126}Te = 0.28 \pm 0.22$ and [Te] = 6839 ± 1041 μg/g.

$$\Delta^{128/126}Te = \delta^{128/126}Te_{residue} - \delta^{128/126}Te_{initial} \qquad (3)$$

where $\delta^{128/126}Te_{initial}$ represents the Te isotope composition of the mean composition of the measured starting materials and $\delta^{128/126}Te_{residue}$ represents the Te isotope composition of the respective Te evaporation experiment.

3. Results

3.1. Tellurium concentrations and isotopic compositions

The Te concentrations and stable isotope compositions of the evaporation experiments, starting glasses, and pure Te oxide (measured by MC-ICP-MS) are reported in Table 1 and are shown in Fig. 2. The depletion of Te in the residue glasses relative to the composition of the bulk starting glass is reported as $\log(f_{Te})$, where $f_{Te} = [Te]^{residue}/[Te]^{initial}$. Over the entire range of experimental conditions from 868 to 1459 °C, $\log(f_{Te})$ varies from 0 to −4, which corresponds to absolute concentrations from the starting material (7589 μg/g) to 0.7 μg/g Te, or a loss of up to 99.991% of initial Te. We obtained electron microprobe and LA-ICP-MS profiles on the cross-sectioned samples (e.g. Fig. 1e) of all experiments (full data in electronic supplement). Above 1200 °C we do not observe any Te diffusion profiles, which implies that diffusion is not the rate-limiting factor of Te evaporation at high temperatures.

In the low T runs (≤1250 °C) we observe occasional vesicles (Fig. 1 c). However, we are not able to discern whether these bubbles are remnants from bubbles in the starting glass (Fig. 1a & b), or whether they formed during the evaporation experiments. At higher temperatures the melt viscosity decreases, and no bubbles can be observed in the quenched samples (Fig. 1d).

Between 1000 and 1400 °C the Te loss increases as a function of temperature (Fig. 2b). However, above 1400 °C, no further Te depletion in the samples with increasing temperatures is observed. At the FMQ buffer, $\log(f_{Te})$ does not further decrease from 1350 to 1500 °C and reaches a minimum in the range of −4 to −3.3, which

is equal to 1.1–3.9 μg/g in absolute Te concentrations. With increasing temperature, the evaporation of Te strongly depends on the oxygen fugacity of the experiments, where $\log(f_{Te})$ decreases with increasing fO_2, and Te is most volatile in experiments run in air (Fig. 2a).

The evaporation experiments exhibit an overall Te isotope variation of ∼1‰/amu ($\Delta^{128/126}Te$ of −0.45 to 1.42) in the residual glasses. Experiments performed at 868–1012 °C and three of the experiments performed at 1181 °C (a, e, f) show loss of up to ∼80% Te that is accompanied by Te isotope fractionation toward lighter isotopic compositions (i.e., $\Delta^{128/126}Te$ from 0.04 to −0.40), defining a linear correlation in a diagram of $\Delta^{128/126}Te$ versus log (f_{Te}) (Fig. 2c). Both Te isotope fractionation and loss are functions of temperature, where the experiments performed at 1181 °C exhibit higher degrees of Te loss (f_{Te} of ∼0.20–0.30) and larger Te isotope fractionation than experiments performed at 868 and 1012 °C.

At ∼1200 °C the isotopic fractionation behavior changes and the residue becomes increasingly heavier in $\Delta^{128/126}Te$ with increasing temperature up to 1400 °C (Fig. 2d). However, at temperatures from 1353 to 1459 °C $\Delta^{128/126}Te$ does not further increase, with the highest $\Delta^{128/126}Te = 1.47$ at 1353 °C and at the FMQ buffer.

The relationship between the isotopic fractionation $\Delta^{128/126}Te$ and the oxygen fugacity relative to the FMQ buffer is shown in Fig. 3. At 868–1181 °C and at 1353 °C the Te isotopic composition is not correlated with the oxygen fugacity, while at 1274 °C $\Delta^{128/126}Te$ increases with increasing fO_2. However, this is likely a result of the strong decrease in $\log(f_{Te})$ in these experiments (Fig. 2a), which in turn controls $\Delta^{128/126}Te$ (Fig. 2c).

4. Discussion

4.1. Tellurium congruent dissociative evaporation

The evaporation mechanism of Te from the silicate melt depends on the chemical evaporation reaction (Sossi et al., 2019), which requires knowledge about the speciation of Te in the gas phase and the silicate melt. We calculate the gas phase speciation of Te, Se and S in a CO-CO_2 atmosphere at 1 bar and 1200 °C over a $\log fO_2$ range from −24 to 0, by Gibbs free energy minimization using the software package HSC Chemistry 9 (2018, Metso:Outotec) (Fig. 4, calculation results in Supplement 2). The models contain 1 mol% Te, Se, and S respectively. The low concentrations were chosen to model the behavior of the metals as traces in the CO-CO_2 atmosphere. The calculation indicates that below $\log fO_2 = -4$ the dominant Te gas species is Te_2, with a minor contribution of Te. In both gas species Te has an oxidation state of 0. At $\log fO_2 = -3.1$ ($\Delta FMQ+5.3$) and above, the oxidation state of Te increases and $Te^{4+}O_2$ becomes the dominant Te gas species at highly oxidizing conditions, such as in air. The change in Te oxidation state and speciation is comparable to that of Se, where the speciation change to SeO_2 occurs at $\log fO_2 = -4.2$ (1200 °C, 1 bar, $\Delta FMQ+4.2$). In contrast, S remains oxidized in the gas phase as SO_2 to much lower oxygen fugacities and the speciation in a water-free system changes to S_2 and COS at $\log fO_2 = -10.3$ (1200 °C, 1 bar), which is equivalent to $\Delta FMQ-1.9$ (Fig. 4).

The redox dependent speciation of Te in aluminosilicate melts and glasses is unconstrained and data is needed. We infer the speciation and oxidation state of Te by comparison with the better constrained chalcogens S and Se. For S, X-ray absorption near-edge spectroscopy (XANES) identified two species, S^{6+} at oxidizing conditions above $\Delta FMQ+1$, and S^{2-} below (Jugo et al., 2010; Wilke et al., 2011). The two species coexist only over a narrow fO_2 range, where S has a solubility minimum in natural and synthetic glasses (Backnaes and Deubener, 2011). Sulfur changes its oxidation state from reduced to oxidized in silicate melts at ∼3 $\log fO_2$ units above

Table 1
Experimental conditions and results. In the text and figures we report the results as log(f_Te), where f_Te is the ratio of Te concentrations in the experiments to the glass powder starting material DB02 (f_Te = [Te]^residue/[Te]^initial). Isotopic compositions are reported as $\Delta^{128/126}$Te.

Lab-ID	Sample label	Temp.[a] (°C)	Weight (mg)	Log (f_O2)	ΔFMQ	Aliquot[b] (%)	Te(μg/g) (±2σ)	N[c]	δ^{128/126}Te (±2s.d.)[d]	[Te]^residue/[Te]^initial (±2σ)	log (f_Te)	+2s. d.	−2s. d.	Δ^{128/126}Te (±2s.d.)
Te oxide														
DB01	Te-ox_1		6.3			0.1		5	0.42 ± 0.02					0.13 ± 0.22
DC01	Te-ox_2		8.7			0.1		4	0.43 ± 0.01					0.14 ± 0.22
Starting material														
DB02	Glass powder		20.6			1.0	7589 ± 139	5	0.33 ± 0.01	1.11 ± 0.17	0.05	0.06	0.07	0.05 ± 0.22
CO01	Glass_1		11.9			0.5	6311 ± 175	5	0.09 ± 0.02	0.92 ± 0.14	−0.03	0.06	0.07	−0.19 ± 0.22
DB03	Glass_2		24.0			1.0	6580 ± 110	5	0.30 ± 0.01	0.96 ± 0.15	−0.02	0.06	0.07	0.02 ± 0.22
CR01	Glass_3		9.3			1.0	6562 ± 183	5	0.37 ± 0.03	0.96 ± 0.15	−0.02	0.06	0.07	0.09 ± 0.22
DB04	Glass_4		13.6			1.0	7154 ± 145	5	0.31 ± 0.02	1.05 ± 0.16	0.02	0.06	0.07	0.03 ± 0.22
Initial mean (±2s.d.)							*6839 ± 1041*	*5*	*0.28 ± 0.22*					
Experiments at 868 °C														
DB05	Te_868a	868 ± 5	8.1	−0.68	12.09	1.0	5874 ± 110	5	0.22 ± 0.02	0.86 ± 0.13	−0.07	0.06	0.07	−0.07 ± 0.22
DB06	Te_868c	868 ± 5	8.2	−12.77	0.00	1.0	7661 ± 159	5	0.32 ± 0.01	1.12 ± 0.17	0.05	0.06	0.07	0.04 ± 0.22
Experiments at 1012 °C														
DB07	Te_1012a	1012 ± 5	11.7	−0.68	9.68	1.0	4573 ± 70	5	0.21 ± 0.01	0.67 ± 0.10	−0.17	0.06	0.07	−0.07 ± 0.22
DB08	Te_1012b	1012 ± 5	8.4	−8.86	1.50	1.0	7237 ± 127	5	0.19 ± 0.01	1.06 ± 0.16	0.02	0.06	0.07	−0.09 ± 0.22
DB09	Te_1012c	1012 ± 5	14.4	−10.36	0.00	1.0	5679 ± 75	5	0.18 ± 0.01	0.83 ± 0.13	−0.08	0.06	0.07	−0.10 ± 0.22
DB10	Te_1012d	1012 ± 5	10.1	−12.36	−2.00	1.0	6519 ± 95	5	0.29 ± 0.01	0.95 ± 0.15	−0.02	0.06	0.07	0.00 ± 0.22
DB11	Te_1012e	1012 ± 5	15.7	−14.36	−4.00	1.0	4141 ± 55	5	0.07 ± 0.01	0.61 ± 0.09	−0.22	0.06	0.07	−0.22 ± 0.22
DB12	Te_1012f	1012 ± 5	18.0	−16.36	−6.00	1.0	5801 ± 109	4	0.23 ± 0.01	0.85 ± 0.13	−0.07	0.06	0.07	−0.06 ± 0.22
Experiments at 1181 °C														
CO08	Te_1181a	1181 ± 5	19.3	−0.68	7.73	1.1	1507 ± 64	5	−0.09 ± 0.01	0.22 ± 0.03	−0.66	0.06	0.07	−0.38 ± 0.22
CO09	Te_1181b	1181 ± 5	5.5	−6.91	1.50	1.7	1053 ± 31	5	0.24 ± 0.01	0.15 ± 0.02	−0.81	0.06	0.07	−0.04 ± 0.22
DB13	Te_1181c	1181 ± 5	9.1	−8.41	0.00	5.0	1326 ± 34	4	0.33 ± 0.01	0.19 ± 0.03	−0.71	0.06	0.07	0.04 ± 0.22
CO10	Te_1181d	1181 ± 5	6.2	−10.41	−2.00	1.7	1026 ± 24	5	0.22 ± 0.02	0.15 ± 0.02	−0.82	0.06	0.07	−0.06 ± 0.22
CO11	Te_1181e	1181 ± 5	13.3	−12.41	−4.00	0.5	1905 ± 58	5	−0.12 ± 0.01	0.28 ± 0.04	−0.56	0.06	0.07	−0.40 ± 0.22
CO12	Te_1181f	1181 ± 5	15.9	−14.41	−6.00	0.3	2236 ± 70	5	−0.03 ± 0.03	0.33 ± 0.05	−0.49	0.06	0.07	−0.31 ± 0.22
DB14	Te_1181f (rep.)	1181 ± 5	6.5	−14.41	−6.00	5.0	1331 ± 33	4	0.52 ± 0.02	0.19 ± 0.03	−0.71	0.06	0.07	0.24 ± 0.22
Experiments at 1196 °C														
DB15	Te_1196a	1196 ± 5	27.9	−0.68	7.16	5.0	1364 ± 103	3	0.90 ± 0.01	0.20 ± 0.03	−0.70	0.07	0.08	0.62 ± 0.22
CR02	Te_1196c	1196 ± 5	11.0	−7.84	0.00	5.1	339 ± 6	5	0.81 ± 0.02	0.050 ± 0.008	−1.31	0.06	0.07	0.52 ± 0.22
Experiments at 1274 °C														
CO02	Te_1274a	1274 ± 5	17.6	−0.68	6.62	11	47.6 ± 1.8	5	1.18 ± 0.02	0.0070 ± 0.0011	−2.16	0.06	0.07	0.89 ± 0.22
CO03	Te_1274b	1274 ± 5	7.0	−5.80	1.50	17	71.8 ± 2.2	5	1.15 ± 0.01	0.0105 ± 0.0016	−1.98	0.06	0.07	0.86 ± 0.22
CO04	Te_1274c	1274 ± 5	6.0	−7.30	0.00	32	23.9 ± 0.9	5	1.40 ± 0.02	0.0035 ± 0.0005	−2.46	0.06	0.07	1.12 ± 0.22
CO05	Te_1274d	1274 ± 5	6.7	−9.30	−2.00	8.1	197 ± 5	5	0.58 ± 0.02	0.029 ± 0.004	−1.54	0.06	0.07	0.29 ± 0.22
CO06	Te_1274e	1274 ± 5	6.0	−11.30	−4.00	6.8	361 ± 12	5	0.62 ± 0.02	0.053 ± 0.008	−1.28	0.06	0.07	0.34 ± 0.22
CO07	Te_1274f	1274 ± 5	9.5	−13.30	−6.00	2.5	581 ± 18	5	0.33 ± 0.01	0.085 ± 0.013	−1.07	0.06	0.07	0.05 ± 0.22
Experiments at 1301 °C														
CR03	Te_1301c	1301 ± 5	4.7	−6.79	0.00	100	3.2 ± 1.5	1	0.85 ± 0.03	0.00047 ± 0.00023	−3.33	0.17	0.29	0.56 ± 0.22
Experiments at 1353 °C														
CR04	Te_1353a	1353 ± 5	9.5	−0.68	5.62	100	0.7 ± 0.2	1	1.41 ± 0.03	0.00010 ± 0.00003	−4.01	0.12	0.16	1.12 ± 0.22
CR05	Te_1353b	1353 ± 5	18.2	−4.80	1.50	100	2.0 ± 0.4	1	1.59 ± 0.03	0.00030 ± 0.00007	−3.53	0.09	0.12	1.31 ± 0.22
DB20	Te_1353b (rep.)	1353 ± 5	25.5	−4.80	1.50	100	3.3 ± 0.1	5	1.56 ± 0.03	0.00049 ± 0.00008	−3.31	0.06	0.07	1.28 ± 0.22
CR06	Te_1353c	1353 ± 5	11.2	−6.30	0.00	100	1.1 ± 0.2	1	1.75 ± 0.03	0.00016 ± 0.00004	−3.79	0.09	0.11	1.47 ± 0.22
CR07	Te_1353d	1353 ± 5	8.1	−8.30	−2.00	100	60.3 ± 1.7	5	1.49 ± 0.02	0.0088 ± 0.0014	−2.05	0.06	0.07	1.21 ± 0.22
CR08	Te_1353e	1353 ± 5	7.7	−10.30	−4.00	100	61.3 ± 3.9	5	1.34 ± 0.01	0.0090 ± 0.0015	−2.05	0.07	0.08	1.06 ± 0.22
CR09	Te_1353f	1353 ± 5	12.1	−12.30	−6.00	100	13.3 ± 3.9	5	1.50 ± 0.03	0.0019 ± 0.0006	−2.71	0.13	0.18	1.21 ± 0.22
Experiments at 1408 °C														
DB22	Te_1408a	1408 ± 5	14.4	−0.68	5.16	100	1.4 ± 0.1	1	1.36 ± 0.03	0.00020 ± 0.00003	−3.69	0.06	0.07	1.08 ± 0.22
CR10	Te_1408c	1408 ± 5	10.3	−5.84	0.00	100	1.1 ± 0.1	1	1.28 ± 0.03	0.00016 ± 0.00003	−3.80	0.06	0.08	0.99 ± 0.22
DB23	Te_1408c (rep.)	1408 ± 5	27.1	−5.84	0.00	100	3.6 ± 0.2	4	1.46 ± 0.03	0.00053 ± 0.00009	−3.28	0.07	0.08	1.18 ± 0.22
Experiments at 1459 °C														
CR11	Te_1459c	1459 ± 5	8.5	−5.40	0.00	100	1.8 ± 0.3	1	1.44 ± 0.03	0.00026 ± 0.00006	−3.59	0.09	0.12	1.15 ± 0.22
DB24	Te_1459c (rep.)	1459 ± 5	35.0	−5.40	0.00	100	3.9 ± 0.2	5	1.39 ± 0.01	0.00056 ± 0.00009	−3.25	0.07	0.08	1.11 ± 0.22

[a] Corrected sample temperature.
[b] Aliquot used for Te isotope measurements using MC-ICPMS.
[c] Number of analyses of the same sample digestion.
[d] For single measurements (n = 1) a maximum uncertainty of ±0.03 was estimated based on samples that were measured multiple times (n = 3–5).

the reduced to oxidized transition in the gas phase speciation (ΔFMQ+1 vs ΔFMQ−1.9). Selenium is reduced as Se^{2-} below an oxidation transition in the range of ΔFMQ+1 – ΔFMQ+4 to Se^{4+}, followed by an additional oxidation step to Se^{6+} above ΔFMQ+9 (Wykes, 2014). Since Te changes its oxidation state in the gas phase

at a similar fO_2 as Se, we infer that the redox change in the silicate melt from Te^{2-} to Te^{4+} occurs at a similar fO_2 around ΔFMQ+2 to ΔFMQ+6. We therefore suggest the evaporation reaction of Te at $fO_2 >$ ΔFMQ+4 as:
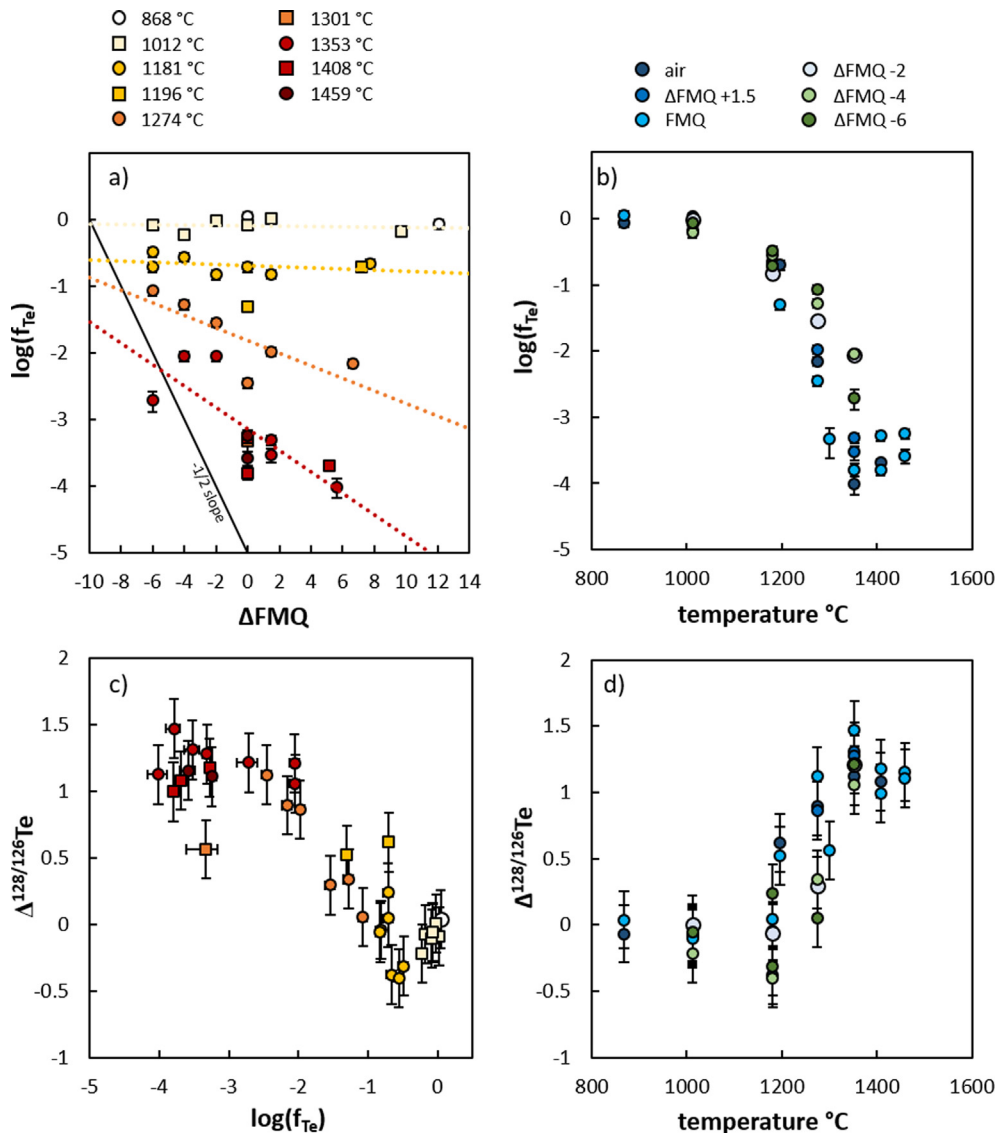
Fig. 2. Experimental results from Te evaporation experiments from silicate melts. (a) Logarithm of the fraction of undegassed Te to the starting material after 15 min as a function of fO$_2$ shown relative to the FMQ buffer. (b) log(f_{Te}) as a function of temperature, where the colors of the symbols denote the fO$_2$ relative to FMQ. (c) Stable isotope fractionation of Te as a function of log(f_{Te}). (d) Stable isotope fractionation of Te as a function of temperature.

$$Te^{4+}O_{2(l)} \rightarrow Te^{4+}O_{2(g)} \tag{4}$$

This reaction applies to the experiments conducted at high fO$_2$ in air (experiment series a). We follow the theoretical description by Sossi et al. (2019, 2020) for the evaporation of cation oxides:

$$\ln\left(\frac{X_{Te}^t}{X_{Te}^0}\right) = \frac{-K^*}{f(O_2)^{\frac{n}{4}}} \frac{3M}{r\rho} \sqrt{\frac{1}{2\pi M_{TeO_2}RT}}(t - t_0) \tag{5}$$

where n is the number of electrons exchanged in the evaporation reaction (n = 0 for Eq. (4)), r is the radius of the melt sphere, ρ the density of the melt, M the molar mass of the melt, M_{TeO_2} the molar mass of the gas species, R the gas constant, T the absolute temperature, t the duration of the experiment, and t_0 the delay between the start of the experiment and the onset of evaporation (see details on the calculation in Supplement 1). K* is the modified equilibrium constant of the reaction (4), where $K^* = K\alpha_{ev}\gamma_{Te}$ (K is the equilibrium constant of the reaction, α_{ev} is the Langmuir evaporation coefficient and γ_{Te} is the activity coefficient of TeO$_2$ in the melt). The modified equilibrium constant K* increases exponen-

tially with temperature in the Te evaporation experiments in air, as shown in Fig. 5a. The Langmuir evaporation coefficient (α_{ev}) and the TeO$_2$ activity coefficient in the melt (γ_{Te}) are unknowns and unconstrained by our experiments. However, Fig. 5 demonstrates that the theoretical model by Sossi et al. (2019, 2020), which is based the Hertz-Knudsen-Langmuir equation, is a good fit to our data on TeO$_2$ degassing from silicate melts at oxidizing condition.

At high temperatures (>1200 °C), where concentration profiles through the samples showed no diffusion profiles (Fig. 1), we may assume that TeO$_2$ evaporation is rate limited only by the evaporation reaction (4). We can, therefore, calculate a kinetic isotopic fractionation factor α_K for the evaporation of TeO$_2$ from the melt at oxidizing conditions in air, by obtaining the slope of the data between ln(f_{Te}) and 1000ln[(1 + 10$^{-3}\delta^{128/126}$Te$_{res}$)/ (1 + 10$^{-3}\delta^{128/126}$Te$_{ini}$)], as shown in Fig. 5b. The slope is equal to 1000(1-α_K), and we obtain α_K = 0.99993 at 1196–1408 °C in air.

At fO$_2$ conditions below ΔFMQ+2, Te evaporates as Te$_2$ according to the reaction:

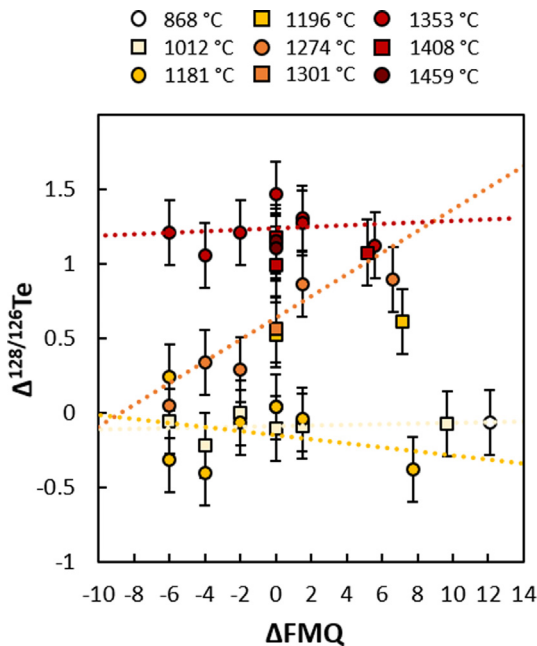$$2Te_{(l)}^{2-} + O_{2(g)} \rightarrow Te_{2(g)}^0 + 2O_{(l)}^{2-} \tag{6}$$

Fig. 3. Tellurium stable isotope fractionation as a function of fO_2 relative to the FMQ buffer. Linear regressions represent best fits through data of experiments performed at a given temperature.

In this case, Te^{2-} replaces O^{2-} on the anion sublattice of the melt. Since Eq. (6) contains charged species, it is referred to as a pseudo-equilibrium. The abundance of O^{2-} far exceeds that of Te^{2-} in the melt. Under equilibrium conditions, the Te solubility is predicted to be proportional to $(fTe_2/fO_2)^{1/2}$. This relationship corresponds to the dissolution of reduced S^{2-} in silicate melts, described by the sulfide capacity C_S (Fincham and Richardson, 1954; O'Neill and Mavrogenes, 2002; Wykes et al., 2015). Accordingly, the telluride capacity C_{Te} may be defined as:

$$\log C_{Te} = \log[Te] + \frac{1}{2}\log(fO_2/fTe_2) \qquad (7)$$

However, the Te evaporation experiments do not determine the telluride capacity, indicated by the discrepancy between the data and the slope of $-1/2$ of the Te concentration versus the oxygen fugacity (Fig. 2a). Instead, the data show that Te has not fully evaporated from the melt in most experiments. At very high temperatures > 1400 °C we observe no further decrease in Te concentrations in the experiments. For example, the experiments at FMQ show no decrease in the concentration from 1301 to 1459 °C (Fig. 2b). We interpret this as the absolute minimum residual solubility of Te^{2-} at FMQ in our B-bearing An-Di eutectic melt under these conditions.

The kinetic isotopic fractionation factor α_K of the evaporation from the melt is proportional to the slope of the isotopic data relative to the degree of volatile loss as shown in Fig. 2c. However, for the experiments at $\log fO_2 \leq FMQ+1.5$, where Te evaporates as Te_2, we do not observe a simple relationship. In these experiments, the evaporation is not a simple loss of a metal cation or oxide component, but the replacement of Te^{2-} by O^{2-} on the anion sublattice (see above). This suggests, that the evaporation of Te from silicate melts is not described by a single mechanism. A mechanistic explanation of this mechanism will require the determination of the coordination and bonding environment of Te^{2-} in silicate melts and glasses by X-ray absorption spectroscopy.

4.2. Low temperature evaporation behavior

Above, we primarily discussed the Te evaporation and isotopic fraction at high temperatures ≥ 1250 °C, where $\Delta^{128/126}Te$

increases with decreasing Te concentration. However, at lower temperatures <1250 °C we observe an inverse behavior, where $\Delta^{128/126}Te$ decreases upon evaporation of up to 80% of the initial Te content (Fig. 2c). Similarly, we have observed a decrease in $\delta^{128/126}Te$ from the Te-oxide starting material (TeO_2) to the synthesized glass that we used for the experiments (Table 1). As the starting material glass was prepared at 1200 °C, we suggest that this may a related process at temperatures below 1250 °C, where heavy Te is preferably lost. In the low temperature experiments the rate of Te evaporation from the melt is not controlled by the evaporation reaction, but by the diffusion of Te from the interior of the melt bead to the surface. If we only consider the experiments where diffusion appears to control the evaporation rate, and exclude experiments in air, we can calculate an isotopic fractionation factor α_{lowT}, in a similar fashion to the high-temperature experiments in air (Fig. 5b). These experiments include Te_868c, Te_1012b, Te_1012c, Te_1012d, Te_1012e, Te_1012f, and Te_1181f. We obtain an isotopic fractionation factor of α_{lowT} = 1.00028. However, the overall limited decrease in $\Delta^{128/126}Te$ is barely resolved when considering the uncertainty on $\Delta^{128/126}Te$ (0.22‰, ±2s.d.) due to the heterogeneity of the starting material (Table 1 and Fig. 2).

The quantitative interpretation of this observation is barred by a lack of structural information on the role of Te in silicate melts and glasses. A detailed investigation of the bonding environment of Te in silicate melts, including melt speciation and coordination, is required to explain the observed isotopic fractionation. We expect that the structural behavior is similar to that of S, however, redox dependent changes in the speciation occur at higher fO_2 for Te, as suggested by the gas-phase speciation (Fig. 4).

5. Implications

The volatility of Te decreases with decreasing fO_2, as demonstrated by our experiments (Fig. 2a). This key finding has important implications for the understanding of Te behavior at reducing conditions, such as in the case of the Moon. At the reducing conditions estimated for lunar magmatic rocks (FMQ−3.3 to FMQ−6; Wadhwa, 2008) we predict a lower volatility for Te, compared to the more oxidizing conditions in terrestrial volcanism. This is in agreement with observations from lunar mafic impact melt breccias, which show little to no evaporation and loss of Te, Se and S, despite the high energies involved in large events such as the Imbrium basin forming impact (Gleißner and Becker, 2020). The processes occurring in the plumes of large-scale impact events remain poorly understood. However, the limited evaporation of volatile elements like Te suggests that oxidation of gases, vapors or melts in these processes is unlikely. Furthermore, since we observe a strong increase of Te volatility with temperature above 1200 °C (Fig. 2b), limited evaporation could imply rapid cooling of the impacted material.

A notable decoupling of Te from S occurs in some volatile element enriched lunar samples, commonly referred to as "Rusty Rocks", such as sample 66095 (Krähenbühl et al., 1973; Shearer et al., 2012, 2014; Gargano et al., 2020). In the "Rusty Rock" a fumarolic gas metasomatized the impact melt breccia introducing sulfides and chlorides at temperatures of about 580 °C (Renggli and Klemme, 2021). However, in contrast to S, no significant enrichment of Te and Se is observed in 66095 and similarly altered samples such as 60016 and 65095 (Krähenbühl et al., 1973; Jean et al., 2016). This decoupling of chalcogens may either be due to a depletion of Te and Se in the source of the fumarolic gas, relative to S, or evaporation may have occurred at an fO_2 where only S is volatile, likely at more elevated fO_2. This redox dependent difference between S and Te is predicted by the gas phase speciation
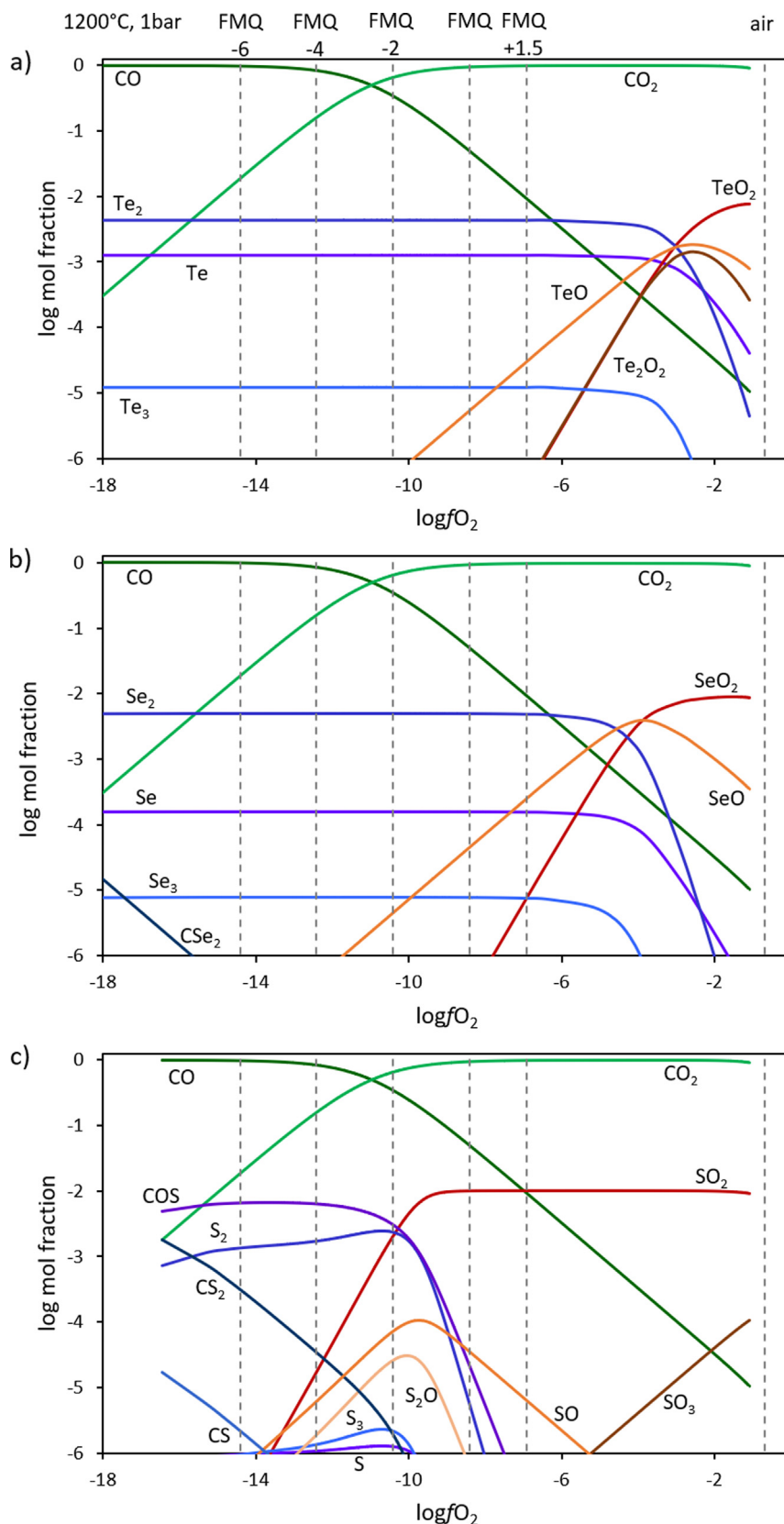
Fig. 4. Gas phase speciation of the chalcogen elements at 1200 °C, 1 bar, in a CO-CO$_2$ atmosphere, as a function of logfO$_2$. The vertical stippled lines indicate the oxygen fugacities of the Te evaporation experiments in air, and relative to the FMQ buffer. (a) Te; TeO$_2$ is the predominant gas species at very high oxygen fugacities, whereas Te$_2$ is the most abundant gas species at lower fO$_2$. (b) Se; the transition from oxidized gas species (SeO$_2$) to reduced species (Se$_2$) occurs at slightly lower logfO$_2$, compared to Te. (c) S; The speciation change of S occurs at much lower logfO$_2$ (~FMQ−2) compared to Te and Se. The complete speciation results at 1050, 1200, and 1300 °C are provided in Supplement 2.
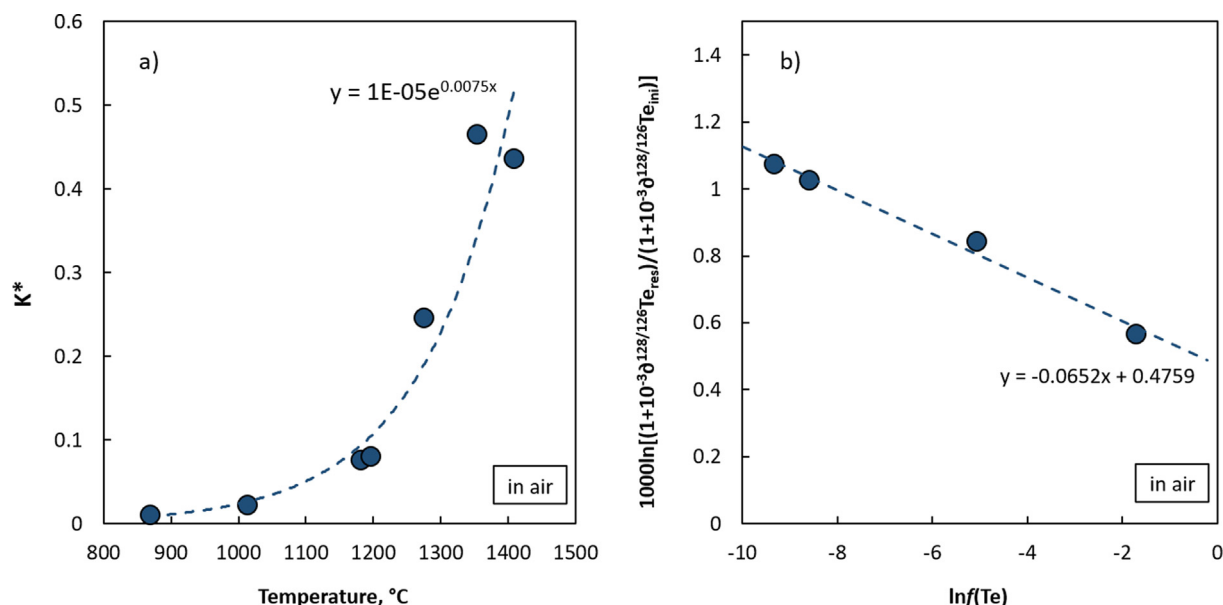
Fig. 5. (a) Modified equilibrium constant K* (Eq. (5)) of reaction (4) for the evaporation of TeO_2 from a melt at oxidizing conditions (in air) as a function of temperature. (b) Relationship between $\ln(f_{Te})$ vs $1000\ln[(1 + 10^{-3}\delta^{128/126}Te_{res})/(1 + 10^{-3}\delta^{128/126}Te_{ini})]$ for experiments in air at 1196–1408 °C. The slope in the data relates to $1000(1 - \alpha_K)$, where α_K is the kinetic isotope fractionation between TeO_2 in the gas phase and the residual TeO_2 in the melt ($\alpha_K = 0.99993$).

(Fig. 4) and remains to be tested for the speciation of Te in silicate melts by X-ray spectroscopic methods. On the other hand, the highest Te abundance measured in a 66095 anorthosite leachate (0.28 ppm Te) corresponds to the most Zn rich sample (66095, 425B L) (Day et al., 2017). This is evidence for some Te mobility in the "Rusty Rock" fumarolic gas.

A natural analog of the evaporation experiments are chondrules, micrometer-to-millimeter-sized spherules that are a major constituent of chondrites. Although there is no consensus about the exact processes that were involved in the formation of chondrules (Russell et al., 2018), it is commonly assumed that chondrules formed as free floating melt droplets by transient heating events in the solar nebula and have undergone temperatures of >1300 °C (Libourel and Portail, 2018). As such, they potentially were subject to evaporative loss of volatile elements. While no Te isotope data exist for chondrules of non-carbonaceous chondrites, Hellmann et al. (2020) inferred a light Te isotope signature for chondrules in carbonaceous chondrites relative to CI chondrites (which are considered to be chemically representative of Solar System's matter). This observation is in contrast to theoretical considerations suggesting an isotopically heavy composition of chondrules as a result of evaporative Te loss. Thus, it has been concluded that the light Te isotope signature was most likely established during condensation of the chondrule precursors or during re-condensation of volatile elements into chondrules (Hellmann et al., 2020). Our new experimental data may shed new light on this issue. For temperatures >1300 °C, comparable to those during chondrule formation, the degassing experiments reveal significant Te loss and associated Te isotope fractionation towards heavier isotope compositions in the residues. Similar to theoretical considerations, this observation is in contrast to evaporative loss of Te during chondrule formation, and provides further evidence that the volatile budget in carbonaceous chondrite chondrules was established during (re-)condensation. However, for degassing experiments performed at temperatures <1200 °C, Te loss resulted in preferential loss of heavy Te isotopes from the melt. Although the cause of this isotope fractionation behavior remains unclear, the low temperature experiments demonstrate the feasibility of light isotopic compositions in residual melts as the result of evaporative Te loss. It is possible that a similar process affected the Te

isotope composition of chondrules. Finally, given that chondrule formation presumably took place under different pressure conditions and chondrules have distinct chemical compositions from the experimental glasses, it remains difficult to assess whether Te isotope fraction during chondrule formation was mainly controlled by Te diffusion in the melt or congruent dissociative evaporation.

Data availability

All data is included in the manuscript and supplementary material.

Declaration of Competing Interest

The authors declare that they have no known competing financial interests or personal relationships that could have appeared to influence the work reported in this paper.

Appendix A. Supplementary material

Supplementary material to this article can be found online at https://doi.org/10.1016/j.gca.2022.10.032.

References

Backnaes, L., Deubener, J., 2011. Experimental Studies on Sulfur Solubility in Silicate Melts at Near-Atmospheric Pressure. Rev. Mineral. Geochem. 73, 143–165.

Braukmüller, N., Wombacher, F., Hezel, D.C., Escoube, R., Münker, C., 2018. The chemical composition of carbonaceous chondrites: Implications for volatile element depletion, complementarity and alteration. Geochim. Cosmochim. Acta 239, 17–48.

Day, J.M.D., Moynier, F., Shearer, C.K., 2017. Late-stage magmatic outgassing from a volatile-depleted Moon. Proc. Natl. Acad. Sci. 201708236.

Fehr, M.A., Hammond, S.J., Parkinson, I.J., 2018. Tellurium stable isotope fractionation in chondritic meteorites and some terrestrial samples. Geochim. Cosmochim. Acta 222, 17–33.

Fincham, C.J.B., Richardson, F.D., 1954. The behaviour of sulphur in silicate and aluminate melts. Proc. R. Soc. Lond. Ser. Math. Phys. Sci. 223, 40–62.

Gargano, A., Sharp, Z., Shearer, C., Simon, J.I., Halliday, A., Buckley, W., 2020. The Cl isotope composition and halogen contents of Apollo-return samples. Proc. Natl. Acad. Sci. 202014503.

Gleißner, P., Becker, H., 2020. New constraints on the formation of lunar mafic impact melt breccias from S-Se-Te and highly siderophile elements. Meteorit. Planet. Sci. 55, 2044–2065.

Gleißner, P., Salme, J., Becker, H., 2022. Siderophile volatile element inventory in lunar magmatic rocks and mantle sources. Earth Planet. Sci. Lett. 593, 117680.

Grundler, P.V., Brugger, J., Etschmann, B.E., Helm, L., Liu, W., Spry, P.G., Tian, Y., Testemale, D., Pring, A., 2013. Speciation of aqueous tellurium(IV) in hydrothermal solutions and vapors, and the role of oxidized tellurium species in Te transport and gold deposition. Geochim. Cosmochim. Acta 120, 298–325.

Hellmann, J.L., Hopp, T., Burkhardt, C., Kleine, T., 2020. Origin of volatile element depletion among carbonaceous chondrites. Earth Planet. Sci. Lett. 549, 116508.

Hellmann, J.L., Hopp, T., Burkhardt, C., Becker, H., Fischer-Gödde, M., Kleine, T., 2021. Tellurium isotope cosmochemistry: Implications for volatile fractionation in chondrite parent bodies and origin of the late veneer. Geochim. Cosmochim. Acta 309, 313–328.

Henley, R.W., Berger, B.R., 2013. Nature's refineries — Metals and metalloids in arc volcanoes. Earth-Sci. Rev. 125, 146–170.

HSC Chemistry 9 [Computer software] (2018) Metso:Outotec. http://www.mogroup.com/portfolio-chemistry/.

Jean, M.M., Bonder, B., Farley, C., Taylor, L.A., 2016. Rusty Rocks" from the Moon: Volatile-Element Contributions from Meteorites. In: Lunar and Planetary Science Conference, p. 2498.

Jugo, P.J., Wilke, M., Botcharnikov, R.E., 2010. Sulfur K-edge XANES analysis of natural and synthetic basaltic glasses: Implications for S speciation and S content as function of oxygen fugacity. Geochim. Cosmochim. Acta 74, 5926–5938.

Kadlag, Y., Becker, H., 2015. Fractionation of highly siderophile and chalcogen elements in components of EH3 chondrites. Geochim. Cosmochim. Acta 161, 166–187.

Kadlag, Y., Becker, H., 2016a. 187Re–187Os systematics, highly siderophile element, S–Se–Te abundances in the components of unequilibrated L chondrites. Geochim. Cosmochim. Acta 172, 225–246.

Kadlag, Y., Becker, H., 2016b. Highly siderophile and chalcogen element constraints on the origin of components of the Allende and Murchison meteorites. Meteorit. Planet. Sci. 51, 1136–1152.

Kadlag, Y., Becker, H., 2017. Origin of highly siderophile and chalcogen element fractionations in the components of unequilibrated H and LL chondrites. Geochemistry 77, 105–119.

Klemme, S., Genske, F., Sossi, P.A., Berndt, J., Renggli, C.J., Stracke, A., 2022. Cr stable isotope fractionation by evaporation from silicate melts. Chem. Geol. 610, 121096.

Krähenbühl, U., Ganapathy, R., Morgan, J.A., Anders, E., 1973. Volatile elements in Apollo 16 samples: implications for highland volcanism and accretion history of the moon. In: Proceedings of the 4th Lunar Science Conference. Pergamon Press, New York, pp. 1325–1348.

Libourel, G., Portail, M., 2018. Chondrules as direct thermochemical sensors of solar protoplanetary disk gas. Sci. Adv.

Lissner, M., König, S., Luguet, A., le Roux, P.J., Schuth, S., Heuser, A., le Roex, A.P., 2014. Selenium and tellurium systematics in MORBs from the southern Mid-Atlantic Ridge (47–50°S). Geochim. Cosmochim. Acta 144, 379–402.

Lodders, K., 2003. Solar System Abundances and Condensation Temperatures of the Elements. Astrophys. J. 591, 1220.

Lorand, J.-P., Alard, O., 2010. Determination of selenium and tellurium concentrations in Pyrenean peridotites (Ariege, France): New insight into S/Se/Te systematics of the upper in mantle samples. Chem. Geol. 278, 120–130.

Neuman, M., Holzheid, A., Lodders, K., Fegley, B., Jolliff, B.L., Koefoed, P., Chen, H., Wang, K., 2022. High temperature evaporation and isotopic fractionation of K and Cu. Geochim. Cosmochim. Acta 316, 1–20.

Nielsen, S.G., Shu, Y., Wood, B.J., Blusztajn, J., Auro, M., Norris, C.A., Wörner, G., 2021. Thallium Isotope Fractionation During Magma Degassing: Evidence From Experiments and Kamchatka Arc Lavas. Geochem. Geophys. Geosyst. 22. e2020GC009608.

Norris, C.A., Wood, B.J., 2017. Earth's volatile contents established by melting and vaporization. Nature 549, 507–510.

O'Neill, H.S.C., Mavrogenes, J.A., 2002. The Sulfide Capacity and the Sulfur Content at Sulfide Saturation of Silicate Melts at 1400°C and 1 bar. J. Petrol. 43, 1049–1087.

Palme, H., O'Neill, H.S.C., 2014. Cosmochemical Estimates of Mantle Composition. In: Holland, H.D., Turekian, K.K. (Eds.), Treatise on Geochemistry. 2nd ed. Elsevier, Oxford, pp. 1–39.

Pangritz, P., Renggli, C.J., Berndt, J., Rohrbach, A., Klemme, S., 2022. Synthesis of Large Amounts of Volatile Element-Bearing Silicate Glasses Using a Two-Stage Melting Process. ACS Earth Space Chem.

Pierazzo, E., Vickery, A.M., Melosh, H.J., 1997. A Reevaluation of Impact Melt Production. Icarus 127, 408–423.

Regelous, M., Regelous, A., Grasby, S.E., Bond, D.P.G., Haase, K.M., Gleißner, S., Wignall, P.B., 2020. Tellurium in Late Permian-Early Triassic Sediments as a Proxy for Siberian Flood Basalt Volcanism. Geochem. Geophys. Geosyst. 21. e2020GC009064.

Renggli, C.J., Klemme, S., 2021. Experimental Investigation of Apollo 16 "Rusty Rock" Alteration by a Lunar Fumarolic Gas. J. Geophys. Res. Planets 126. e2020JE006609.

Renggli, C.J., Klemme, S., 2020. Experimental constraints on metal transport in fumarolic gases. J. Volcanol. Geotherm. Res. 400, 106929.

Richter, F.M., Janney, P.E., Mendybaev, R.A., Davis, A.M., Wadhwa, M., 2007. Elemental and isotopic fractionation of Type B CAI-like liquids by evaporation. Geochim. Cosmochim. Acta 71, 5544–5564.

Richter, F.M., Dauphas, N., Teng, F.-Z., 2009. Non-traditional fractionation of non-traditional isotopes: Evaporation, chemical diffusion and Soret diffusion. Chem. Geol. 258, 92–103.

Richter, F.M., Mendybaev, R.A., Christensen, J.N., Ebel, D., Gaffney, A., 2011. Laboratory experiments bearing on the origin and evolution of olivine-rich chondrules. Meteorit. Planet. Sci. 46, 1152–1178.

Russell, S.S., Connolly Jr., H.C., Krot, A.N. (Eds.), 2018. Chondrules: Records of Protoplanetary Disk Processes. 1st ed. Cambridge University Press.

Shearer, C.K., Burger, P.V., Guan, Y., Papike, J.J., Sutton, S.R., Atudorei, N.-V., 2012. Origin of sulfide replacement textures in lunar breccias. Implications for vapor element transport in the lunar crust. Geochim. Cosmochim. Acta 83, 138–158.

Shearer, C.K., Sharp, Z.D., Burger, P.V., McCubbin, F.M., Provencio, P.P., Brearley, A.J., Steele, A., 2014. Chlorine distribution and its isotopic composition in "rusty rock" 66095. Implications for volatile element enrichments of "rusty rock" and lunar soils, origin of "rusty" alteration, and volatile element behavior on the Moon. Geochim. Cosmochim. Acta 139, 411–433.

Siebert, Christopher, Nägler, Thomas F., Kramers, Jan D., 2001. Determination of molybdenum isotope fractionation by double-spike multicollector inductively coupled plasma mass spectrometry. Geochemistry Geophysics Geosystems 2. https://doi.org/10.1029/2000GC000124.

Sossi, P.A., Klemme, S., O'Neill, H., St, C., Berndt, J., Moynier, F., 2019. Evaporation of moderately volatile elements from silicate melts: experiments and theory. Geochim. Cosmochim. Acta 260, 204–231.

Sossi, P.A., Moynier, F., Treilles, R., Mokhtari, M., Wang, X., Siebert, J., 2020. An experimentally-determined general formalism for evaporation and isotope fractionation of Cu and Zn from silicate melts between 1300 and 1500 °C and 1 bar. Geochim. Cosmochim. Acta 288, 316–340.

Tombros, S., Seymour, K.St., Williams-Jones, A.E., 2010. Controls on Tellurium in Base, Precious, and Telluride Minerals in the Panormos Bay Ag-Au-Te Deposits, Tinos Island, Cyclades, Greece. Econ. Geol. 105, 1097–1111.

Tombros, S.F., Fitros, M., 2019. Evidence for vapor transport of the base and precious metals in the Panormos Bay Ag-Au-Te deposit, Tinos Island, Cyclades. J. Geochem. Explor. 199, 128–140.

Wadhwa, M., 2008. Redox Conditions on Small Bodies, the Moon and Mars. Rev. Mineral. Geochem. 68, 493–510.

Wang, K., Jacobsen, S.B., 2016. Potassium isotopic evidence for a high-energy giant impact origin of the Moon. Nature 538, 487–490.

Warren, P.H., 2008. Lunar rock-rain: Diverse silicate impact-vapor condensates in an Apollo-14 regolith breccia. Geochim. Cosmochim. Acta 72, 3562–3585.

Wilke, M., Klimm, K., Kohn, S.C., 2011. Spectroscopic Studies on Sulfur Speciation in Synthetic and Natural Glasses. Rev. Mineral. Geochem. 73, 41–78.

Wimpenny, J., Marks, N., Knight, K., Rolison, J.M., Borg, L., Eppich, G., Badro, J., Ryerson, F.J., Sanborn, M., Huyskens, M.H., Yin, Q., 2019. Experimental determination of Zn isotope fractionation during evaporative loss at extreme temperatures. Geochim. Cosmochim. Acta 259, 391–411.

Wimpenny, J., Marks, N., Knight, K., Borg, L., Badro, J., Ryerson, F., 2020. Constraining the behavior of gallium isotopes during evaporation at extreme temperatures. Geochim. Cosmochim. Acta 286, 54–71.

Wombacher, F., Rehkämper, M., Mezger, K., 2004. Determination of the mass-dependence of cadmium isotope fractionation during evaporation. Geochim. Cosmochim. Acta 68, 2349–2357.

Wood, B.J., Smythe, D.J., Harrison, T., 2019. The condensation temperatures of the elements: A reappraisal. Am. Mineral. 104, 844–856.

Wykes, J.L., 2014. Selenium and sulfur in silicate melts. Australian National University. PhD Thesis.

Wykes, J.L., O'Neill, H.S.C., Mavrogenes, J.A., 2015. The Effect of FeO on the Sulfur Content at Sulfide Saturation (SCSS) and the Selenium Content at Selenide Saturation of Silicate Melts. J. Petrol. 56, 1407–1424.

Yi, W., Halliday, A.N., Alt, J.C., Lee, D.-C., Rehkämper, M., Garcia, M.O., Langmuir, C.H., Su, Y., 2000. Cadmium, indium, tin, tellurium, and sulfur in oceanic basalts: Implications for chalcophile element fractionation in the Earth. J. Geophys. Res. Solid Earth 105, 18927–18948.

Yierpan, A., Redlinger, J., König, S., 2021. Selenium and tellurium in Reykjanes Ridge and Icelandic basalts: Evidence for degassing-induced Se isotope fractionation. Geochim. Cosmochim. Acta 313, 155–172.

Young, E.D., Shahar, A., Nimmo, F., Schlichting, H.E., Schauble, E.A., Tang, H., Labidi, J., 2019. Near-equilibrium isotope fractionation during planetesimal evaporation. Icarus 323, 1–15.

Zelenski, M., Simakin, A., Taran, Y.u., Kamenetsky, V.S., Malik, N., 2021. Partitioning of elements between high-temperature, low-density aqueous fluid and silicate melt as derived from volcanic gas geochemistry. Geochim. Cosmochim. Acta 295, 112–134.